

Excited-state band structure mapping

M. Puppin,^{1,2} C. W. Nicholson,³ C. Monney,³ Y. Deng,⁴ R. P. Xian,² J. Feldl,² S. Dong,²
A. Dominguez,^{5,6} H. Hübener,⁷ A. Rubio,^{7,8,9} M. Wolf,² L. Rettig,² and R. Ernstorfer^{2,10}

¹*Laboratoire de Spectroscopie Ultrarapide and
Lausanne Centre for Ultrafast Science (LACUS),
cole Polytechnique Fdrale de Lausanne, ISIC,
Station 6, CH-1015 Lausanne, Switzerland*

²*Fritz-Haber-Institut der Max-Planck-Gesellschaft,
Faradayweg 4-6, 14195 Berlin, Germany**

³*Department of physics and Fribourg centre for nanomaterials,
University of Fribourg, Chemin du Muse 3, CH-1700 Switzerland*

⁴*Paul Scherrer Institute, SwissFEL, 5232 Villigen PSI, Switzerland*

⁵*Shenzhen JL Computational Science and Applied
Research Institute, Shenzhen, 518131 China*

⁶*Beijing Computational Science Research Center, Beijing 100193, China*

⁷*Max Planck Institute for the Structure and Dynamics
of Matter and Center for Free Electron Laser Science,
Luruper Chaussee 149, Geb. 99 (CFEL), 22761 Hamburg*

⁸*Center for Computational Quantum Physics,
Flatiron Institute, 162 5th Ave., New York, 10010 NY, USA*

⁹*Nano-Bio Spectroscopy Group, Universidad del
País Vasco UPV/EHU- 20018 San Sebastin, Spain*

¹⁰*Institut für Optik und Atomare Physik, Technische Universitt Berlin,
Strae des 17. Juni 135, 10632 Berlin, Germany†*

(Dated: August 17, 2021)

Abstract

Angle-resolved photoelectron spectroscopy is an extremely powerful probe of materials to access the occupied electronic structure with energy and momentum resolution. However, it remains blind to those dynamic states above the Fermi level that determine technologically relevant transport properties. In this work, we extend band structure mapping into the unoccupied states and across the entire Brillouin zone by using a state-of-the-art high repetition rate, extreme ultraviolet femtosecond light source to probe optically excited samples. The wide-ranging applicability and power of this approach are demonstrated by measurements on the 2D semiconductor WSe₂, where the energy-momentum dispersion of valence and conduction bands are observed in a single experiment. This provides a direct momentum-resolved view not only on the complete out-of-equilibrium band gap but also on its renormalization induced by electron-hole interaction and screening. Our work establishes a new benchmark for measuring the band structure of materials, with direct access to the energy-momentum dispersion of the excited-state spectral function.

Functionality in electronic and optoelectronic devices is based on the control of the flow of charge carriers under out-of-equilibrium conditions. At the microscopic level, charge transport and device operation rely upon generating non-equilibrium electron distributions controlled by external fields to achieve the desired electronic response. The propagation of electrons in a crystal and the evolution of their energy distributions are governed by the details of the electronic structure as well as the efficiency of elastic and inelastic scattering processes.

Time-resolved ARPES (trARPES) addresses this problem by observing the spectral function of a material after excitation via a femtosecond optical pulse [1]. The momentum-resolved distribution of excited states combined with the dynamical information on state lifetimes provides a powerful view into excited solids [2], extending the scope of ARPES and allowing to observe out-of-equilibrium electronic properties which can be used to extract the electronic coupling with phonons and other degrees of freedom [3, 4]. Ultimately, understanding matter out-of-equilibrium is mandatory for achieving optical control in complex materials [5]. TrARPES can resolve states unoccupied at equilibrium, and has been used to reveal the unoccupied band structure of topological materials [6], to measure optically-

* michele.puppini@epfl.ch

† ernstorfer@fhi-berlin.mpg.de

dressed states [7], to observe spin-valley polarizations in the conduction band of transition metal dichalcogenide semiconductors [8] and has enabled the direct observation of excitons [2, 9, 10].

An important open question is how band properties extracted from the trARPES spectral function in the excited state compare with conventional steady-state experiments, e.g. optical spectroscopy or ARPES. A common expectation is that a comparison is possible in the weak excitation limit [11] where trARPES experiment become very challenging, particularly when accessing the full Brillouin zone (BZ) of the investigated material. This is beyond the reach of most trARPES experiments, which are performed at ultraviolet (UV) photon energies. Extending these experiments to the extreme-ultraviolet (XUV) photon energy range and correspondingly to high photoelectron momenta covering the whole BZ, while retaining a comparable signal-to-noise ratio and weak excitation densities have been challenging until the recent development of suitable high-repetition-rate XUV sources [11–15].

In this work, we employ a state-of-the-art experimental setup [12] to simultaneously determine the energy of conduction states (unoccupied at equilibrium) and valence states. This allows us to address the band gap, one of the fundamental opto-electronic properties, by mapping in reciprocal space both valence and conduction bands of 2H-WSe₂, a two-dimensional transition metal dichalcogenide (TMD) semiconductor widely studied for excitonic and spin-valleytronic applications [16–18].

The conduction band population is probed with a 21.7 eV XUV pulse following photoexcitation by a 3.1 eV pulse, with a temporal resolution better than 100 fs. Excited-state ARPES measurements are performed before energy relaxation to the conduction band minimum and reveal the energy versus momentum dispersion of valence and conduction states in a single experiment. We then study the excited-state band gap and its renormalization due to many-body effects and demonstrate that in the low-excitation limit the trARPES gap agrees with the band gap measured by other spectroscopies and predicted by theory. This validates excited-state band structure mapping as a generally applicable method to measure, with momentum resolution, the conduction states of materials.

To better understand the difference and similarities between ARPES and trARPES, we shortly review the two experimental approaches. In an ARPES experiment, a photon with energy $h\nu$ excites a single-crystalline sample, and the kinetic energy E of photoelectrons is measured along a wavevector direction \mathbf{k} . If photoionization is treated as a sudden process,

the photoemission intensity can be approximated as [19]:

$$I(\mathbf{k}, E) = I_0(\mathbf{k}, E)A^-(\mathbf{k}, E)f_{\mu,T}(E). \quad (1)$$

Equation 1, which for simplicity neglects the experimentally finite angular and energy resolution, as well as charge transport at the surface, links the ARPES spectrum $I(\mathbf{k}, E)$ to the underlying electronic structure via three factors. The one-electron-removal spectral function, $A^-(\mathbf{k}, E)$, contains the information about the quasi-particle band structure and many-body interactions. The spectral weight is modulated by a matrix element term $I_0(\mathbf{k}, E)$, which depends on initial and final state symmetry and wave vectors, as well as photon energy ($h\nu$) and polarization, and the experimental geometry [20, 21]. Thirdly, the Fermi-Dirac distribution $f_{\mu,T}(E)$ imposes that only states populated at the temperature T can contribute to the measured spectrum, setting a limit to the highest accessible energy to few $k_B T$ above the chemical potential μ . The matrix element term is vanishing unless momentum conservation parallel to the sample's surface is fulfilled by the escaping photoelectron, allowing to link the measured photoelectron angular distribution $I(\mathbf{k}, E)$ to the quasi-particle bands in reciprocal space, as illustrated in Fig. 1 a). Parallel momentum (\mathbf{k}_{\parallel}) conservation, together with energy conservation, imposes that typically only energetic photons in the XUV range can access the whole BZ [22]. As an example, photons with an energy of ≈ 20 eV are necessary to measure the first BZ boundary of WSe₂, as indicated by the violet dashed line in Fig. 1 a). In our experiment photoelectron spectra are collected with a hemispherical energy analyser (HEA) which measures kinetic energy (E_K) and angle of emission along the entrance slit (Fig. 1 b), this corresponds to a line-cut throughout the function $I(\mathbf{k}, E)$ (full green lines in Fig. 1 a). Band mapping is achieved by angular scanning of the sample (green arrows in Fig. 1 a) and b) across the analyser slit. The multi-dimensional function $I(\mathbf{k}, E)$ is constructed from different images and data can be displayed as constant energy cuts or as energy versus momentum plots, as shown in Fig. 1 a) where a horizontal constant energy cut close to the valence band maximum and a vertical energy versus momentum dispersion across the BZ are plotted. It is worth noting the alternative approach of momentum microscopy, in which the whole accessible photoemission space is collected at the same time [23]. A detailed comparison between the two methods reveals that an HEA ensures higher counting statistics when acquiring data along a specific direction [24], whereas the fixed geometry provided by momentum microscopy is suitable for the

study of the symmetry-dependent matrix element $I_0(\mathbf{k}, E)$ [21].

A time-resolved ARPES experiment accesses an excited state of the material by performing an ARPES experiment at a well-defined temporal delay t following a femtosecond optical pump pulse (1 b). The trARPES spectrum $\tilde{I}(\mathbf{k}, E, t)$ thereby measures the (quasi)-electron-removal spectrum as a function of this time delay:

$$\tilde{I}(\mathbf{k}, E, t) = \tilde{I}_0(\mathbf{k}, E, t)\tilde{A}^-(\mathbf{k}, E, t)\tilde{f}(\mathbf{k}, E, t). \quad (2)$$

Here eq. 1 is modified to include the explicit time dependence of each term. The optical excitation produces not only an out-of-equilibrium electronic distribution \tilde{f} , but also perturbs the many-body interactions in the spectral term \tilde{A}^- . The matrix element term \tilde{I}_0 can become a time-dependent quantity if the symmetry of the initial or final states is modified [25]. We follow the convention that for $t > 0$ the pump excitation occurs before photoemission: recovery of equilibrium requires that $\tilde{I}(\mathbf{k}, E, t) \xrightarrow{t \rightarrow +\infty} I(\mathbf{k}, E)$.

As illustrated in Fig. 1 b, trARPES provide access to states unoccupied at equilibrium. This can be understood as a two-step process, where, in a first step the femtosecond pump pulse creates an optical polarization in allowed momentum and energy regions, corresponding to vertical optical transitions in the material ($\Delta\mathbf{k} = 0$) [26]. In a second step, microscopic scattering events within a few hundred femtoseconds redistribute electronic population to multiple states across the conduction band (CB) (Fig. 1 a). Electrons relax their excess energy via multiple electron-phonon scattering events towards the band edges and accumulate at the CB minima on time scales typically shorter than a few picoseconds. By measuring the photoelectron energy and angular distribution before significant energy relaxation to the lattice has occurred, the information encoded in \tilde{A}^- can be revealed in a range $E < \mu + h\nu_p$, where $h\nu_p$ is the pump photon energy.

Excited-state band mapping of unoccupied states is particularly demanding and strongly benefits from high repetition rate (> 100 kHz) XUV sources. First, a sufficiently short XUV pulse is fundamental for accessing the out-of-equilibrium state before its decay throughout the BZ. In addition, space charge effects, which are inherent in ARPES with short XUV pulses, are mitigated in high repetition rate experiments [27]. Furthermore, the higher the pump excitation energy density, the stronger many-body interactions modify the function $\tilde{I}(\mathbf{k}, E, t)$ relative to the equilibrium case. trARPES experiments at high-repetition rates benefit from higher counting statistics and hence data can be acquired at weaker perturbation

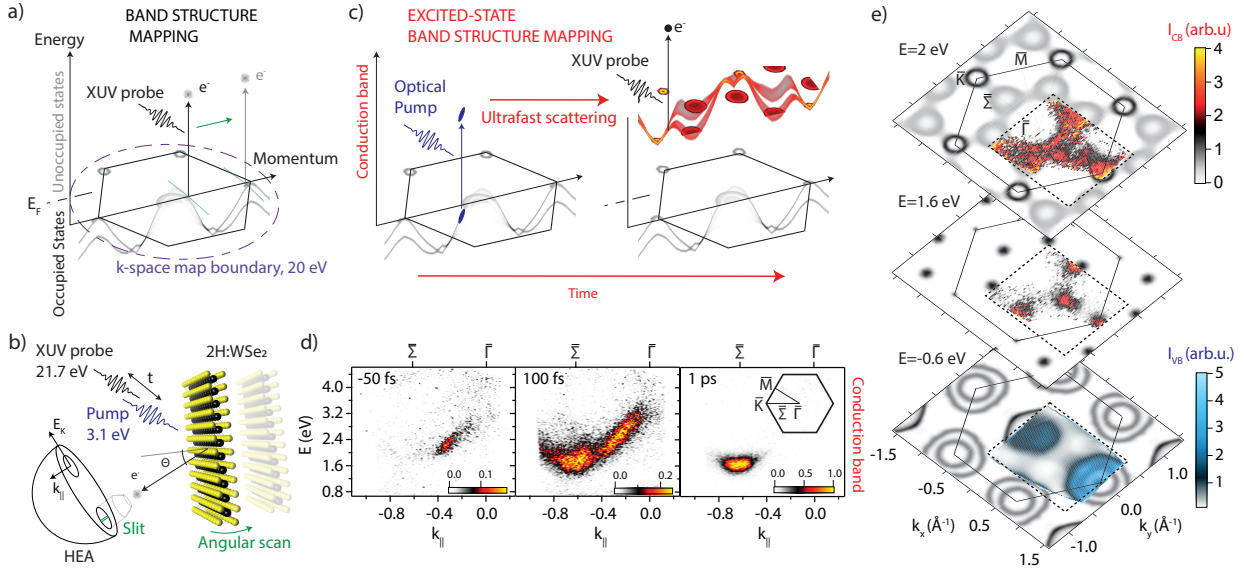


FIG. 1. a) Band structure mapping in reciprocal space by angle-resolved photoelectron spectroscopy (ARPES). The reciprocal space region measured by the hemispherical energy analyser (HEA) for two sample tilt angles is indicated by a green line, the maximum parallel momentum which can be accessed by 20 eV photons is indicated by a violet dashed line. b) trARPES experiments on 2H-WSe₂: an optical pump pulse at an energy of 3.1 eV excites the system. At a delay t , an XUV probe pulse at an energy of 21.7 eV generates photoelectrons, which are measured as a function of the emission angle θ with a HEA. The sample angle is scanned across the analyser slit to collect ARPES maps. c) Excited-state band structure mapping d) trARPES data collected in the conduction band of WSe₂ for pump-probe delays of -50 fs, 100 fs and 1 ps. Inset: the surface Brillouin zone of WSe₂. e) Photoelectron intensity distribution as a function of parallel momentum for three energies at a pump-probe delay of 100 fs; VB and CB energy distribution curves have been independently intensity normalized for better visualization. The experimental data is collected in a region delimited by the dashed line. Outside this region, the results of G_0W_0 calculations are displayed, the theoretical bands dispersion along the k_z direction was integrated; the conduction bands was rigidly offset by a *scissor operator* to match the experimental energy.

strength.

To meet the simultaneous requirements of an ultrashort XUV source with a high repetition rate, in this work we generate probe pulses by high-harmonic generation with an optical parametric chirped pulse amplifier operating at 500 kHz [28]. This results in XUV pulses

at an energy of 21.7 eV and with characteristic time-bandwidth product of approximately $20 \text{ fs} \times 110 \text{ meV}$ [12], which are temporally short enough to access the excited states before significant carrier energy relaxation has occurred and, at the same time, have an energy bandwidth sufficiently narrow to resolve the excited-state energy features. trARPES experiments were performed on single-crystalline samples of bulk WSe_2 , cleaved in ultra-high vacuum conditions. The material was excited by a pump pulse with a photon energy of 3.1 eV and at an excitation energy density of $40 \mu\text{J}/\text{cm}^2$.

To illustrate the ability of trARPES to visualize states which are unoccupied at equilibrium, we show in Fig. 1 d) energy versus momentum data collected in an energy window in the conduction band (CB) along the high symmetry direction $\bar{\Gamma}-\bar{K}$. Three selected time delays (-50 fs, 100 fs and 1 ps) are plotted side by side. The surface BZ of WSe_2 , with the high symmetry points marked, is shown as an inset of Fig. 1 d). During the rising edge of the pump pulse (-50 fs), the CB signal is localized at -0.35 \AA^{-1} from the BZ center ($\bar{\Gamma}$ point). This suggests that in this region population is transferred via an optical transition at the photon energy of 3.1 eV, rather than indirectly by scattering. The intensity of this feature as a function of time was used as a measure of the pump-probe temporal cross-correlation and the temporal maximum was used to define the time zero. The full-width at half maximum of the cross-correlation is 95 fs, dominated by the pump pulse duration [29]. Throughout this work, the zero energy was set for convenience to the valence band energy at the \bar{K} point, the corner of the hexagonal BZ.

At a time delay of 100 fs, population can be observed throughout the conduction states, up to at an energy $\approx 2.5 \text{ eV}$ (Fig. 1 d), central panel). This delay was selected to perform the excited-state band structure mapping. Relaxation towards the Σ conduction band valley minimum is indeed already apparent at a delay of 1 ps (Fig. 1 d), right panel).

An energy window from -1.5 to 3.5 eV was selected to observe simultaneously valence and conduction bands around the band gap, which is a unique feature of trARPES. Three exemplary constant energy cuts of the data at $t = 100 \text{ fs}$ are shown in Fig. 1 e), which display in false colours the photoelectron intensity distribution as a function of parallel momentum for energies of -0.6 eV in the valence band (VB), 1.6 eV and 2 eV in the conduction band (CB). The measurement region is indicated by a dashed line and comprises the whole first BZ of WSe_2 . Two different false color scales are used for conduction and valence states; energy distribution curves were normalized independently in the CB and VB for a clearer

display of the constant energy maps [29].

To rationalize the experimental data we perform *ab initio* density functional theory (DFT) calculations of the electronic band structure using the generalised gradient approximation with the PBE functional, as implemented in the QUANTUM ESPRESSO package [30]. To improve the agreement with experimental data, we use many-body perturbation theory at the one-shot G_0W_0 level [31, 32] on top of DFT results [29]. This computes quasiparticle energies, correcting to lowest order the unscreened electronic Green’s function G_0 by the Coulomb interaction W_0 . The quasi-particle energy dispersion is calculated as a function of the three-dimensional wave-vector (k_x, k_y, k_z) . For a direct comparison with data in Fig. 1 d), the theoretical bands are integrated along the reciprocal space direction orthogonal to the sample surface (k_z). This choice is justified by the strong surface sensitivity of XUV-based photoemission due to the short mean-free-path of photoelectrons. Electron momentum conservation is relaxed for the k_z component, adding an additional source of energy broadening for bands with dispersion out of the surface plane. There is strong evidence that in WSe₂ the photoemission probing depth at 21.7 eV is mostly limited to the uppermost layer (≈ 0.5 nm), in fact, inversion-symmetric WSe₂ surprisingly exhibits strong spin-polarized bands [33] and valley polarization in circularly-pumped tr-ARPES [8]. The importance of final state effects in the material is evidenced by one-step photoemission calculations [21], and will be discussed further below.

The experimental data contains the excited-state CB and VB energy-momentum dispersion for arbitrary reciprocal space directions, which can be compared with our *ab initio* calculations and with other experiments. For this purpose, energy versus momentum photoelectron distributions are plotted along three high-symmetry directions $\bar{\Gamma}$ - $\bar{\Sigma}$ - \bar{K} , \bar{K} - \bar{M} , \bar{M} - $\bar{\Gamma}$ in Fig. 2 and compared with the results of the calculations. The theoretical k_z dispersion is indicated by a shading, highlighting two-dimensional (low k_z dispersion) and three-dimensional states. The experimental photoelectron intensity is plotted without additional normalization, and intensity modulations are attributable to the momentum dependent matrix element. The average intensity of the conduction band signal is a factor 10^{-3} that of the valence states, and we use two distinct false color scales for conduction and valence states, respectively.

The zero energy reference is set to the highest energy VB at the \bar{K} point also for the theoretical data, to minimize any alignment uncertainty due to k_z dispersion. The theoretical

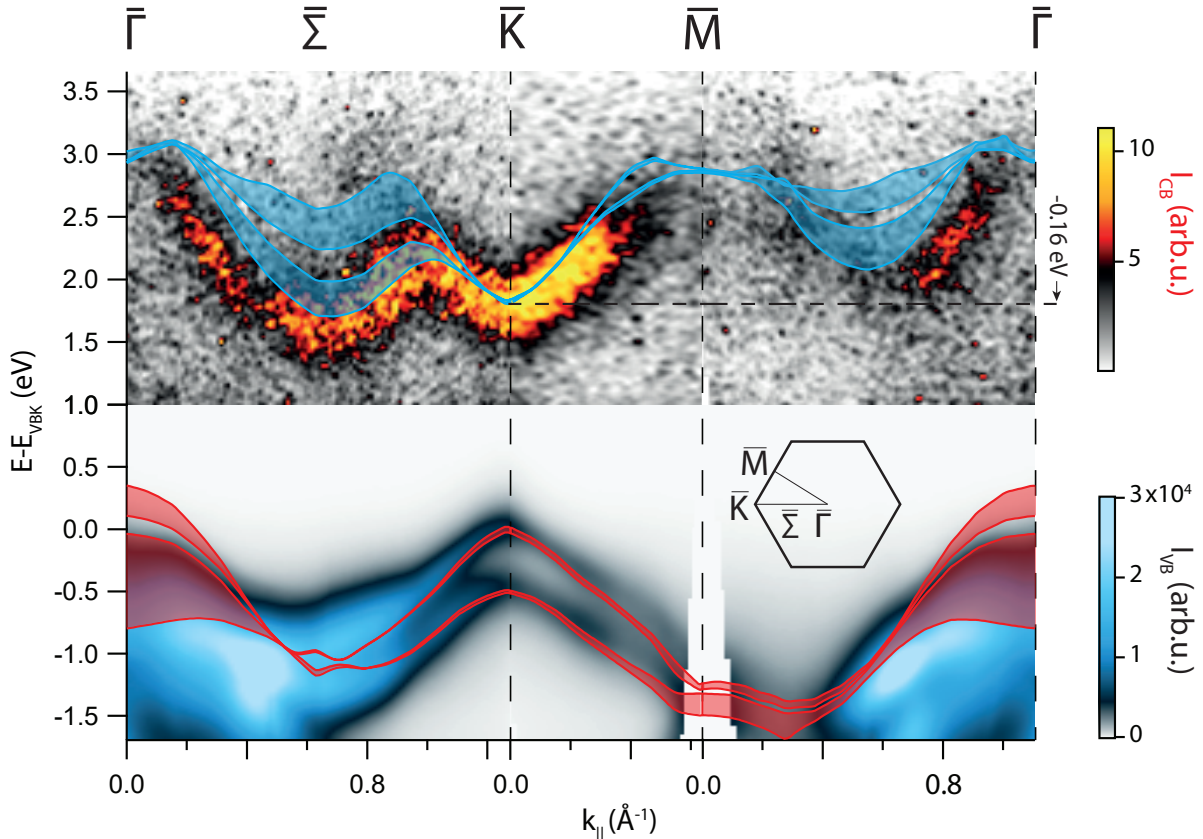


FIG. 2. Measured ARPES intensity as a function of energy and parallel momentum showing the VB and CB along the $\bar{\Gamma}$ - $\bar{\Sigma}$ - \bar{K} , \bar{K} - \bar{M} , \bar{M} - $\bar{\Gamma}$ directions, indicated in the upper panel. Conduction band states are displayed by a different color scale. Blue and red curves indicate the quasiparticle energies calculated with the G_0W_0 method for the CB and VB, respectively. The theoretical band structure energy zero was set to the VB position at the \bar{K} point, the CBs (blue) were rigidly shifted by a -0.16 eV *scissor operator* to match the $\bar{\Sigma}$ valley center energy. The momentum dispersion along the k_z direction is indicated by the shaded area.

conduction states were rigidly shifted by -160 meV to match the measured CB energy at the \bar{K} point, both in Fig. 1 d) and in Fig. 2.

Theory predicts two valence and two conduction bands in the observed energy window, as all calculated bands are spin-degenerate, consistent with the inversion-symmetric bulk crystal structure of 2H-WSe₂. The spin-orbit splitting of the VB band at the \bar{K} point is ≈ 500 meV, in good agreement with past literature [34–36]. Despite being a layered quasi-2D material, WSe₂ displays some inherently three-dimensional features. In particular, the

Σ valley, as well as the valence band at the $\bar{\Gamma}$ point, have considerable k_z dispersion. In contrast, the out-of-plane band dispersion is low in the vicinity of the \bar{K} point, as confirmed by energetically-narrower features in ARPES. Our G_0W_0 calculations predict an orthogonal momentum dispersion on the order of 40 meV for the VB and 30 meV for the CB at the \bar{K} point. Calculations place the indirect band gap between the maximum of the VB at the $\bar{\Gamma}$ point and the Σ valley. In our data the conduction band minimum (CBM) is unambiguously located at the $\bar{\Sigma}$ point, however the apparent valence band maximum (VBM) is observed at the \bar{K} point, and a broad continuum of states is observed at the $\bar{\Gamma}$ point. It is widely accepted that the absolute VB maximum is located at the $\bar{\Gamma}$ point and that matrix element effects cancel the contribution of the upper VB at $\bar{\Gamma}$ [33, 34]. After the rigid offset of -160 meV mentioned above, the G_0W_0 calculations are in qualitative agreement with the excited-state band structure and reproduce the main features of the experimental conduction band.

For a quantitative comparison, the quasi-particle energy must be determined from the ARPES intensity. Final state effects usually complicate the retrieval of quasi-particle energies and of many-body effects in the spectral function. However, the problem is absent in a strictly two-dimensional state (dispersion only along $\mathbf{k}_{\parallel} = (k_x, k_y)$) [37]. Both valence and conduction states at the direct optical band gap at the \bar{K} point are quasi-two-dimensional, enabling for robust comparison of the experimental excited-state band gap with theory and other experimental techniques.

The CB and VB energies are extracted from the experimental data by a fit of the energy distribution curve (EDC) at the \bar{K} point, for $t = 100$ fs. The procedure is illustrated in Fig. 3 a), the photoelectron spectrum of the VB is well fitted by two Gaussian peaks, and by a Shirley background. The two, nearly-degenerate conduction bands predicted by theory are not resolved within the experimental line width, and a single Gaussian peak describes well the CB signal. Due to its higher intensity, the higher energy tail of the VB spectrum appears as a background on the CB, and is modeled by an exponential decay. We define the experimental band gap as the distance between the uppermost VB peak position ($E=0$ by definition) to the center of the CB peak, as highlighted by the red line in Fig. 3 a) and we measure a band gap of 1.76 ± 0.01 eV. We note that this procedure, valid for quasi-2D bands, differs from the method adopted for three-dimensional semiconductors, where the band edge is found by linear extrapolation of the photoelectron spectral edge [38].

The excited-state quasi-particle energy, an out-of-equilibrium quantity, can change as a

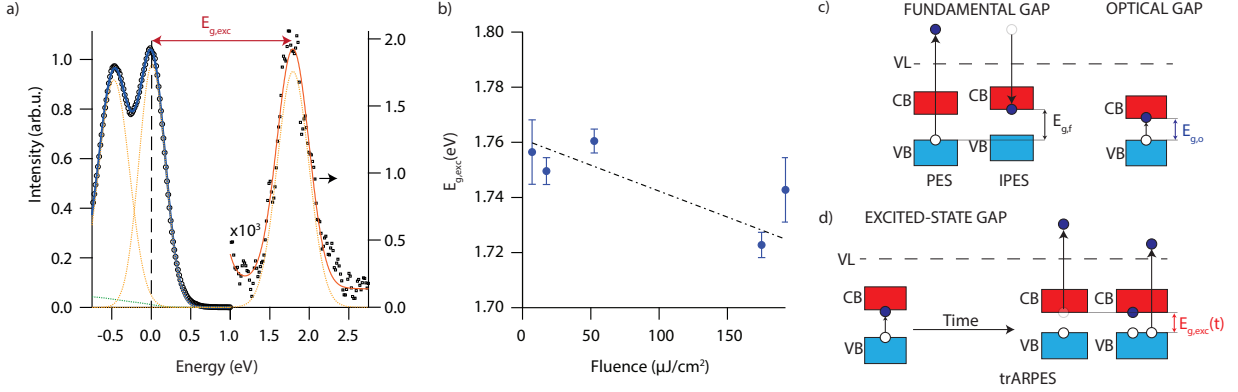


FIG. 3. a) Energy distribution curve at the K point, together with the fit used to determine the excited-state band gap $E_{g,exc}$. The conduction band signal intensity, displayed on the right-hand axis, was scaled by a factor 10^3 for clarity. b) Fluence dependence of the excited-state band gap. c) Schematic comparison between fundamental, optical, and excited-state band gaps, VL indicates the vacuum level.

function of the excitation energy density [39]. To investigate the impact on the band gap, we follow its evolution for increasing incident optical energy density up to $200 \mu\text{J}/\text{cm}^2$ and observe a decrease of the band gap (Fig. 3 b). The maximum effect is $\approx 50 \text{ meV}$, with a linear slope of $1.8 \times 10^{-1} \text{ meV}/(\mu\text{J}/\text{cm}^2)$; the extrapolated limit at zero excitation density is $1.76 \pm 0.03 \text{ eV}$.

It is interesting to compare this experimental band gap, which we call the *excited-state band gap* $E_{g,exc}$, with ab-initio calculations and other experimental techniques. Several experiments have been designed to resolve the electronic structure above the chemical potential [40]. Inverse photoemission [41], scanning tunneling spectroscopy [42], and very low-energy electron diffraction [43] access unoccupied conduction states by adding an electron to the system and probing the complementary one-electron-addition spectral function $A^+(\mathbf{k}, E)$ [44]. Angle-resolved inverse photoemission (ARIPES), in particular, has momentum resolution [40]. Unfortunately, due to the small cross-section of the process and, unlike ARPES, due to the lack of parallel detectors with multiple angular and energy channels, ARIPES has not evolved to a similarly widespread technique [41]. Another approach can be used in photoemission to observe otherwise unoccupied states, namely sample doping by alkali metal atoms [35, 45]. A limitation of alkali doping is the possibility of chemical modification to the band structure [35]. Additionally, resonant inelastic X-ray scattering techniques have

also been used to map the dispersion of unoccupied states [46, 47]. The direct gap at the \bar{K} point for WSe₂ from various methods is displayed in table I.

Method	Band gap (eV)	Reference
ARPES+ARIPES	1.7, 1.4	[34],[48]
ARPES+Doping	1.62	[45]
trARPES	1.76	This work
Optics, A-exciton	1.697*, 1.60, 1.626	[49], [50], [51]
Optics, Interband	1.752*, 1.686	[49], [51]
EELS, A-exciton	1.75	[52]
DFT	1.25, 1.17-1.55	This work, [53–57]
G_0W_0	1.90 , 1.75, 2.08 [‡]	This work, [58], [59]
BSE, A-exciton	1.86 [‡]	[59]
BSE, Interband	2.02 [‡]	[59]

TABLE I. Comparison between experimental (upper part) and theoretical band gap of WSe₂ (lower part) at the \bar{K} point (direct band gap) . *Measured at 77 K, at room temperature the gap is reduced by ≈ 60 meV [51] . [‡] bilayer WSe₂.

The fundamental or quasiparticle band gap $E_{g,f}$ is usually defined as the difference between the electron affinity, i.e. the energy gained by adding a single electron to an N electron system, and the ionization energy, needed to remove an electron leaving N-1 electrons behind [60]. The quasiparticle gap should not be confused with the so-called optical band gap, which will be discussed later on. The so-called transport band gap, determined by electrical transport measurements, coincides with the fundamental band gap, however, in the case of semiconductors such as bulk WSe₂, possessing an indirect band gap and multiple conduction band valleys, momentum-resolved techniques provide a more complete picture. In view of comparison with optical spectroscopy, we restrict here to the case of the direct band gap and we more loosely consider the band gap as a momentum-dependent quantity, which attains its minimum at the direct fundamental band gap. Experimentally, the momentum-dependent quasiparticle band gap can be measured by comparing the VB measured by photoemission (N-1 electron final state) with the CB measured by inverse photoemission (N+1 electrons

final state). This procedure is schematized in Fig. 3 c) and necessitates a common energy reference between the two experimental setups. In particular, the direct fundamental gap of WSe₂ at the \bar{K} point was experimentally measured to be $E_{g,f}^{exp} = 1.7 \pm 0.1$ eV by combining ARPES and ARIPES [34].

When comparing the experimental gap with theoretical results, an important question is to what extent one is allowed to compare *ab initio* calculations such as DFT with energies determined by (time-resolved) photoelectron spectroscopy. DFT computes the ground state electronic density and returns a set of self-consistent Kohn-Sham (KS) bands [61]. Even in an idealized case where the exact density functional is known, a direct comparison between the KS bands and the ARPES measurements is not justified [62]. Nonetheless in many cases, within a constant energy offset, the KS bands are in good agreement with ARPES data of the valence band. For WSe₂, in particular, DFT bands reproduce reasonably well the ARPES VB energy dispersion [33, 34, 36, 63]. However, if $E_{g,f}$ is directly calculated from the KS bands, theory grossly underestimates the band gap. Before applying the G₀W₀ correction, our calculations predict a gap value of 1.25 eV, in line with other DFT results, reported in table I. This well-known *band-gap problem* is intrinsic to DFT [64], and is a reminder that KS energies are indeed not quasi-particle energies. Conversely, Hedin’s GW method [32, 65] can be used to calculate quasiparticle excitations in a solid, such as measured in ARPES (electron removal) or ARIPES (electron addition). GW calculations correct the DFT energies by an approximate electronic self-energy, typically performed to the lowest order (G₀W₀). We find a considerable improvement in the calculated fundamental gap and obtain a value $E_{g,f}^{GW} = 1.90$ eV, in line with previous calculations [58].

A second commonly defined band gap is the so-called *optical band gap* $E_{g,o}$, which corresponds to the lowest energy required for a vertical ($\Delta\mathbf{k} = 0$) electronic transition in the system (Fig. 3 c). This is a neutral excitation where both the initial and final states have N electrons, in contrast with the case of the fundamental gap, which is calculated as the energy difference between an N+1 and an N-1 electrons state. The optical band gap is experimentally measured by optical absorption spectroscopy. A remarkable feature in optical absorption spectra is the appearance of excitonic resonances at energies below the onset of electronic interband transitions. The observation of an excitonic peak is the hallmark of the electron-hole interaction, and its center energy defines the optical band gap. To predict the optical band gap one must solve the Bethe-Salpeter equation [66]. In the optical absorption

spectra of bulk WSe₂ the so-called A exciton is the lowest resonance at an energy of 1.68 eV, the exciton binding energy E_x was determined to be 50 meV, and the inter-band transition has an energy 1.73 eV [49]. This sets the scale for the electron-hole interaction in bulk TMD semiconductors, and one expects $E_{g,o} \approx E_{g,f} - E_x$.

In the *excited-state band gap* measurement (Fig. 3 d), a neutral optical excitation is followed by an ionization step at time t , leading to a N-1 electron excited final state with an additional hole in the VB, which is generated for $t=0$ and is followed by a relaxation dynamics for $t > 0$. The band gap is measured by comparing the kinetic energy of photoelectrons originating from the CB and the VB. Generally speaking, $E_{g,exc}(t)$ is a time-dependent quantity influenced by many-body effects, and can be renormalized by electron-electron interactions, leading to screening and excitonic effects, and by the electron-phonon coupling with the (non-thermal) phonon distribution.

Our data shows that in the low excitation limit, $E_{g,exc}(100 \text{ fs})$ is in good numerical agreement with the fundamental band gap determined by other experiments. Furthermore, we observe no signatures of the A excitonic peak at the \bar{K} point, which appears in optical measurements at a lower energy of $\approx 1.62 \text{ eV}$ [49–51]. A deviation from the single-quasiparticle picture is expected when electron and hole are bound to form excitons [67–69] and photoelectron spectra bear the signature of such interactions as a renormalized energy and momentum dispersion [2, 70]. The agreement with the theoretical G_0W_0 bands in the present case can be rationalized by the fact that the pump photon energy is well above the gap and sufficiently off-resonance to approximate the initial ($t \approx 0$) carrier distribution as an electron-hole plasma, where exciton quasi-particles are not formed [26]. In bulk WSe₂ the formation of stable A excitons at the \bar{K} point is hindered by the possibility of electron (hole) scattering to the $\bar{\Sigma}$ point ($\bar{\Gamma}$ point), which are the global band energy edges. However, if instead the excitation energy is resonant with the excitonic peak observed by optics, excitonic effects can be observed [2].

We note that G_0W_0 calculations overestimate the band gap observed in our out-of-equilibrium experiment by $\approx 160 \text{ meV}$. However, the agreement with the observed band dispersion is still satisfactory upon a rigid shift of the conduction bands to lower photon energies, suggesting that a single-quasiparticle picture holds well for the excited-state band structure in first approximation. Band gap renormalization is expected to occur due to carrier screening and via electron-phonon coupling [39, 71, 72]. Time-resolved diffraction

studies reveal that a non-equilibrium phonon distribution rises on the time scale of a few picoseconds [73]. At a pump-probe delay of 100 fs, where our data was collected, a significant hot phonon population has not yet developed and we conclude that electronic screening must dominate in band structure mapping experiments and we attribute to this effect the observed band gap reduction at higher excitation densities (Fig. 3 b)).

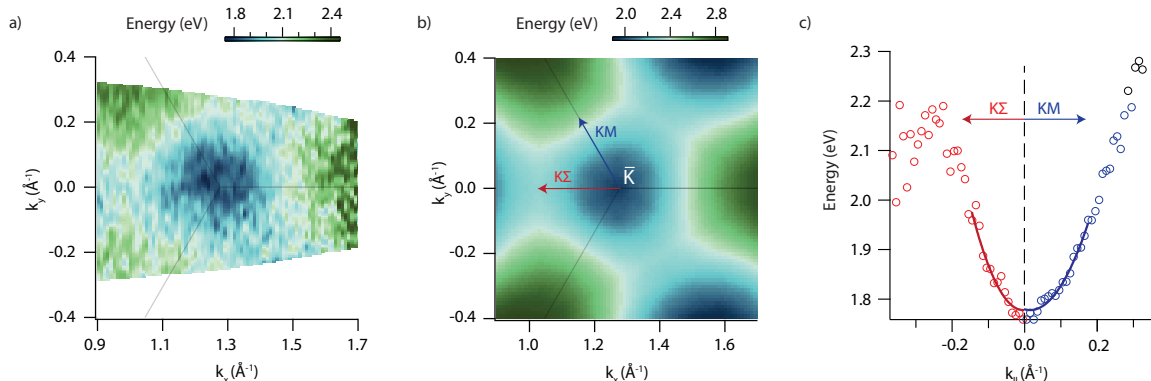


FIG. 4. a) Conduction band center energy at the \bar{K} valley, b) G_0W_0 energy of the K valley c) Dispersion along the directions K- Σ (negative x-axis) and K-M (positive x-axis). The full line indicates the result of parabolic fits to the data.

Having established that the excited-state band gap well approximates the fundamental band gap in our experimental conditions, we now extract the momentum-resolved energy dispersion contained in the experimental maps for the whole 2D \bar{K} valley. The \bar{K} valley energy is shown in Fig. 4 a) and for comparison we plot the theoretical dispersion of the lowest CB in Fig. 4 b). The three-fold symmetry of the valley is evident from the data and the anisotropy of the \bar{K} valley can be quantified by extracting the dispersion along the high-symmetry directions K- Σ and K-M, indicated in Fig. 4 b). For this purpose, we employ the previously described fitting procedure to EDCs surrounding the \bar{K} valley. The band dispersion of both conduction and valence bands was estimated by fitting a parabola in a range of 0.15 \AA^{-1} , as illustrated in Fig. 4 c) for the case of the CB. We obtain a value of $m_e^{K\Sigma} = 0.38 m_0$ ($m_h^{K\Sigma} = -0.52 m_0$) and $m_e^{KM} = 0.55 m_0$ ($m_h^{KM} = -0.56 m_0$) for the CB (VB) in the directions K- Σ and K-M, respectively, where m_0 is the electron mass. The experimental dispersion is somewhat smaller than effective masses reported for DFT, $m_h = -0.625 m_0$ and $m_e = 0.821 m_0$ [74]. Calculated effective masses from DFT depend strongly on computational details and also on the computational band gap [75],

larger theoretical masses might be therefore linked to the underestimation of the gap in the aforementioned work.

By observing hole and electron quasi-particle independently, one can calculate effective ($M = m_e + m_h$) and reduced ($\mu_r = m_e m_h / (m_e + m_h)$) exciton masses. The exciton effective masses are $M^{K\Sigma} = 0.9 m_0$ and $M^{KM} = 1.1 m_0$, which can be compared with experimental results from electron energy loss spectroscopy, $M = 0.91 m_0$ [52] and with optical measurements under magnetic field, which report $M = 0.7 m_0$ [76]. The exciton reduced mass determined from our data is $\mu_r^{K\Sigma} = 0.22 m_0$ and $\mu_r^{KM} = 0.28 m_0$. This can be compared with optical absorption spectroscopy data, from which $\mu_r = 0.21 m_0$ was determined [49]. We stress however that, despite the reasonable numerical agreement, other techniques do not identify the hole and electron masses independently. Furthermore, band anisotropy along different symmetry directions can be readily identified and accounted for within the excited-state band structure. This is particularly relevant for example in valleytronic applications in hetero-layers where energy-degenerate valleys appear at different momentum locations [77]. The detailed effects of layer stacking on the momentum dispersion and on the optical and transport properties is as yet poorly understood and can be directly characterized by excited-state band structure mapping.

The possibility of visualizing the excited-state band structure by trARPES is demonstrated for the TMD WSe₂. The experiment provides simultaneous access to valence and conduction states throughout the BZ thereby completely mapping the material's band gap. The excited-state direct gap at the \bar{K} point agrees in the low-excitation limit with fundamental quasi-particle gap, as obtained by static experiments. Our experiment shows that the excited-state band structure agrees in the low excitation limit with the single-quasiparticle bands and we obtain experimentally conduction and valence band dispersion for the \bar{K} point for various high symmetry directions. Thanks to XUV light sources at high repetition rate, we anticipate that the measurement of the excited-state band structure in the whole BZ can be performed for a broad class of samples. G_0W_0 calculations provide a good qualitative description of the data but predict the experimental out-of-equilibrium band gap only within 160 meV. Excited-state band structure mapping can provide an experimental benchmark to quantitatively fine tune computations, e.g. to accurately predict the band gap in high-throughput computational material discovery for optoelectronic applications [57, 78]. Automated methods for comparison with theory, demonstrated for multi-dimensional ARPES

data [79], are applicable also to excited-state band structure data. Importantly, the method could also provide access to unoccupied states of quantum materials, to resolve topological features above the Fermi level [6], and for correlated materials, e.g. to access the spectral function of unoccupied states in strongly correlated oxides and charge density wave materials [80–82].

ACKNOWLEDGMENTS

This work was funded by the Max-Planck-Gesellschaft, by the German Research Foundation (DFG) within the Emmy Noether program (Grant No. RE 3977/1), and grants FOR1700 (project E5), SPP2244 (project 443366970) and from the European Research Council, Grant Numbers ERC-2015-CoG-682843. M.P. acknowledge financial support by the Swiss National Science Foundation (SNSF) Grant No. CRSK-2_196756. C.W.N. and C.M. acknowledge financial support by the Swiss National Science Foundation (SNSF) Grant No. P00P2_170597. A.R. and H.H acknowledge financial support from the European Research Council (Grant ERC-2015-AdG-694097) and the Cluster of Excellence CUI:Advanced Imaging of Matter of the Deutsche Forschungsgemeinschaft (Grant EXC 2056 Project 390715994).

I. EXPERIMENTAL METHODS

Commercial WSe₂ single crystals were prepared by exfoliation in-situ under UHV conditions. The base pressure during the experiments was below 1×10^{-10} mbar. All the experiments were performed at room temperature, where no surface photovoltage or charging effects were observed. The light source is based on a high-harmonic generation of a high-repetition Ytterbium-based Optical parametric chirped pulse amplifier (OPCPA) [28]. The experiments were performed in an ARPES chamber equipped with a 6-axis manipulator and a hemispherical electron energy analyzer (Specs Phoibos 150), further details on the experimental setup are described in reference [12]. The temporal time zero and pump probe cross correlation of 95 fs were measured by fitting the rising edge of the first observable signal in the excited-state band structure, as illustrated in Fig. 5. The second maximum observed after 100 fs is a result of electron population scattered from other states during the energy relaxation process.

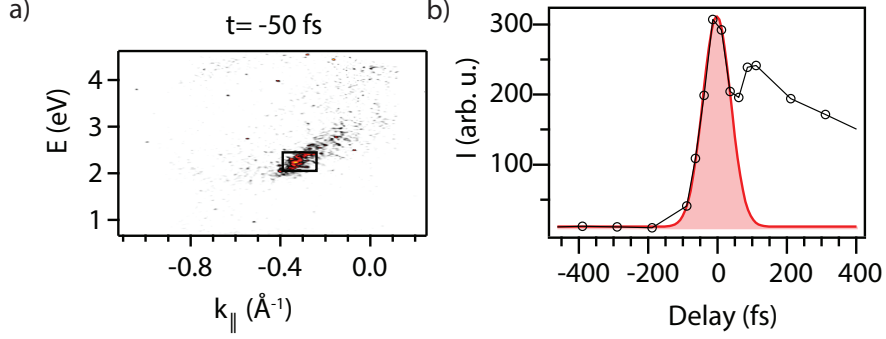


FIG. 5. a) ARPES intensity as a function of energy and parallel momentum showing the conduction states along the $\bar{\Gamma} - \bar{\Sigma}$ direction at a time delay of -50 fs. The pump-probe temporal cross correlation is determined by integrating the signal in the rectangular box. b) Temporal trace showing the integrated intensity in the box of panel a) as function of time. Red curve, Gaussian fit to the rising edge, the FWHM is 95 fs.

II. DATA ANALYSIS

In Fig. 1 e) of the main text, the experimental EDCs have been normalized to the same area as a function of parallel momentum in the VB. This was chosen for reducing the impact of matrix element in the display of constant energy map and for a clearer comparison with the G_0W_0 data. The same procedure was applied to EDCs in the CB (i.e. on the data for $E > 1$ eV), but prior to the area normalization, an exponential background tail from the underlying occupied states was subtracted. No normalization procedure was performed on the data in Fig. 2, Fig. 3 and Fig. 4.

III. THEORETICAL METHODS

The electronic band structure of bulk WSe_2 was computed using many-body perturbation theory at the one-shot G_0W_0 level on top of DFT results. This approach has been vastly employed in the literature for the description of the electronic properties of semiconductor materials due to its accuracy and good agreement with experimental measurements. The system was modelled using a hexagonal supercell with the experimental lattice constants $a = b = 3.28 \text{ \AA}$ and $c = 12.98 \text{ \AA}$ [83]. DFT calculations were performed using the generalised gradient approximation (GGA) with the PBE functional[84]. The Brillouin zone (BZ) was

sampled with a 9x9x9 k-point grid. We used a total of 1000 conduction bands and a 18 Ry energy cutoff for the computation of the inverse dielectric matrix. For the evaluation of the screened and bare Coulomb parts of the self-energy operator, we used energy cutoffs of 18 Ry and 160 Ry, respectively. Spin-orbit coupling was included directly in the DFT calculations and perturbatively at the G_0W_0 level, using the BerkeleyGW package [85]. All employed cutoff values, BZ sampling and number of bands were systematically and independently increased until results were converged within few tens of meV for the conduction and valence band energy difference. Finally, we performed DFT calculations using a 24x24x9 BZ sampling and interpolated linearly the 9x9x9 GW band structure into this finer k-point grid.

-
- [1] C. L. Smallwood, R. A. Kaindl, and A. Lanzara, Ultrafast angle-resolved photoemission spectroscopy of quantum materials, *EPL* **115**, 27001 (2016).
- [2] S. Dong, M. Puppini, T. Pincelli, S. Beaulieu, D. Christiansen, H. Hübener, C. W. Nicholson, R. P. Xian, M. Dendzik, Y. Deng, Y. W. Windsor, M. Selig, E. Malic, A. Rubio, A. Knorr, M. Wolf, L. Rettig, and R. Ernstorfer, Direct measurement of key exciton properties: Energy, dynamics, and spatial distribution of the wave function, *Natural Sciences* **1**, e10010 (2021), <https://onlinelibrary.wiley.com/doi/pdf/10.1002/ntls.10010>.
- [3] U. De Giovannini, H. Hübener, S. A. Sato, and A. Rubio, Direct measurement of electron-phonon coupling with time-resolved ARPES, *Phys. Rev. Lett.* **125**, 136401 (2020).
- [4] M. X. Na, A. K. Mills, F. Boschini, M. Michiardi, B. Nosarzewski, R. P. Day, E. Razzoli, A. Sheyerman, M. Schneider, G. Levy, S. Zhdanovich, T. P. Devereaux, A. F. Kemper, D. J. Jones, and A. Damascelli, Direct determination of mode-projected electron-phonon coupling in the time domain, *Science* **366**, 1231 (2019), <https://science.sciencemag.org/content/366/6470/1231.full.pdf>.
- [5] C. Ahn, A. Cavalleri, A. Georges, S. Ismail-Beigi, A. J. Millis, and J.-M. Triscone, Designing and controlling the properties of transition metal oxide quantum materials, *Nature Materials*, **1** (2021).
- [6] J. A. Sobota, S.-L. Yang, A. F. Kemper, J. J. Lee, F. T. Schmitt, W. Li, R. G. Moore, J. G. Analytis, I. R. Fisher, P. S. Kirchmann, T. P. Devereaux, and Z.-X. Shen, Direct Optical

- Coupling to an Unoccupied Dirac Surface State in the Topological Insulator Bi_2Se_3 , *Physical Review Letters* **111**, 136802 (2013), publisher: American Physical Society.
- [7] Y. H. Wang, H. Steinberg, P. Jarillo-Herrero, and N. Gedik, Observation of Floquet-Bloch States on the Surface of a Topological Insulator, *Science* **342**, 453 (2013).
- [8] S. Meskers, P. van Hal, A. Spiering, J. Hummelen, A. van der Meer, and R. Janssen, Generation and Evolution of Spin-, Valley-, and Layer-Polarized Excited Carriers in Inversion-Symmetric WSe_2 , *Phys. Rev. B* **61**, 9917 (2000), arXiv:1606.03218.
- [9] J. Mado, M. K. L. Man, C. Sahoo, M. Campbell, V. Pareek, E. L. Wong, A. Al-Mahboob, N. S. Chan, A. Karmakar, B. M. K. Mariserla, X. Li, T. F. Heinz, T. Cao, and K. M. Dani, Directly visualizing the momentum-forbidden dark excitons and their dynamics in atomically thin semiconductors, *Science* **370**, 1199 (2020).
- [10] M. K. L. Man, J. Mado, C. Sahoo, K. Xie, M. Campbell, V. Pareek, A. Karmakar, E. L. Wong, A. Al-Mahboob, N. S. Chan, D. R. Bacon, X. Zhu, M. M. M. Abdelrasoul, X. Li, T. F. Heinz, F. H. d. Jornada, T. Cao, and K. M. Dani, Experimental measurement of the intrinsic excitonic wave function, *Science Advances* **7**, eabg0192 (2021), publisher: American Association for the Advancement of Science Section: Research Article.
- [11] J. H. Buss, H. Wang, Y. Xu, J. Maklar, F. Joucken, L. Zeng, S. Stoll, C. Jozwiak, J. Pepper, Y.-D. Chuang, J. D. Denlinger, Z. Hussain, A. Lanzara, and R. A. Kaindl, A setup for extreme-ultraviolet ultrafast angle-resolved photoelectron spectroscopy at 50-kHz repetition rate, *Review of Scientific Instruments* **90**, 023105 (2019), publisher: American Institute of Physics.
- [12] M. Puppini, Y. Deng, C. W. Nicholson, J. Feldl, N. B. M. Schrter, H. Vita, P. S. Kirchmann, C. Monney, L. Rettig, M. Wolf, and R. Ernstorfer, Time- and angle-resolved photoemission spectroscopy of solids in the extreme ultraviolet at 500 kHz repetition rate, *Review of Scientific Instruments* **90**, 023104 (2019), publisher: American Institute of Physics.
- [13] E. J. Sie, T. Rohwer, C. Lee, and N. Gedik, Time-resolved XUV ARPES with tunable 24-33 eV laser pulses at 30 meV resolution, *Nature Communications* **10**, 3535 (2019), number: 1 Publisher: Nature Publishing Group.
- [14] R. Cucini, T. Pincelli, G. Panaccione, D. Kopic, F. Frassetto, P. Miotti, G. M. Pierantozzi, S. Peli, A. Fondacaro, A. De Luisa, A. De Vita, P. Carrara, D. Krizmancic, D. T. Payne, F. Salvador, A. Sterzi, L. Poletto, F. Parmigiani, G. Rossi, and F. Cilento, Coherent nar-

- rowband light source for ultrafast photoelectron spectroscopy in the 17-31 eV photon energy range, *Structural Dynamics* **7**, 014303 (2020), publisher: American Institute of Physics.
- [15] Y. Liu, J. E. Beetar, M. M. Hosen, G. Dhakal, C. Sims, F. Kabir, M. B. Etienne, K. Dimitri, S. Regmi, Y. Liu, A. K. Pathak, D. Kaczorowski, M. Neupane, and M. Chini, Extreme ultraviolet time- and angle-resolved photoemission setup with 21.5 meV resolution using high-order harmonic generation from a turn-key Yb:KGW amplifier, *Review of Scientific Instruments* **91**, 013102 (2020), publisher: American Institute of Physics.
- [16] A. Ciarrocchi, D. Unuchek, A. Avsar, K. Watanabe, T. Taniguchi, and A. Kis, Polarization switching and electrical control of interlayer excitons in two-dimensional van der Waals heterostructures, *Nature Photonics* **13**, 131 (2019), number: 2 Publisher: Nature Publishing Group.
- [17] D. Unuchek, A. Ciarrocchi, A. Avsar, Z. Sun, K. Watanabe, T. Taniguchi, and A. Kis, Valley-polarized exciton currents in a van der Waals heterostructure, *Nature Nanotechnology* **14**, 1104 (2019), number: 12 Publisher: Nature Publishing Group.
- [18] Q. H. Wang, K. Kalantar-Zadeh, A. Kis, J. N. Coleman, and M. S. Strano, Electronics and optoelectronics of two-dimensional transition metal dichalcogenides, *Nature Nanotechnology* **7**, 699 (2012), number: 11 Publisher: Nature Publishing Group.
- [19] A. Damascelli, Angle-resolved photoemission studies of the cuprate superconductors, *Rev. Mod. Phys.* **75**, 473 (2003), arXiv:0208504 [cond-mat].
- [20] S. Moser, An experimentalist's guide to the matrix element in angle resolved photoemission, *J. Electron Spectrosc. Relat. Phenom.* **214**, 29 (2017).
- [21] S. Beaulieu, J. Schusser, S. Dong, M. Schler, T. Pincelli, M. Dendzik, J. Maklar, A. Neef, H. Ebert, K. Hricovini, M. Wolf, J. Braun, L. Rettig, J. Minr, and R. Ernstorfer, Revealing Hidden Orbital Pseudospin Texture with Time-Reversal Dichroism in Photoelectron Angular Distributions, *Physical Review Letters* **125**, 216404 (2020).
- [22] S. Hüfner, *Photoelectron Spectroscopy : Principles and Applications* (Springer Berlin Heidelberg, Berlin, Heidelberg, 2003).
- [23] M. Kotsugi, W. Kuch, F. Offi, L. I. Chelaru, and J. Kirschner, Microspectroscopic two-dimensional Fermi surface mapping using a photoelectron emission microscope, *Review of Scientific Instruments* **74**, 2754 (2003), publisher: American Institute of Physics.

- [24] J. Maklar, S. Dong, S. Beaulieu, T. Pincelli, M. Dendzik, Y. W. Windsor, R. P. Xian, M. Wolf, R. Ernstorfer, and L. Rettig, A quantitative comparison of time-of-flight momentum microscopes and hemispherical analyzers for time- and angle-resolved photoemission spectroscopy experiments, *Review of Scientific Instruments* **91**, 123112 (2020), publisher: American Institute of Physics.
- [25] F. Boschini, D. Bugini, M. Zonno, M. Michiardi, R. P. Day, E. Razzoli, B. Zwartsenberg, M. Schneider, E. H. d. S. Neto, S. d. Conte, S. K. Kushwaha, R. J. Cava, S. Zhdanovich, A. K. Mills, G. Levy, E. Carpene, C. Dallera, C. Giannetti, D. J. Jones, G. Cerullo, and A. Damascelli, Role of matrix elements in the time-resolved photoemission signal, *New Journal of Physics* **22**, 023031 (2020), publisher: IOP Publishing.
- [26] S. W. Koch, M. Kira, G. Khitrova, and H. M. Gibbs, Semiconductor excitons in new light, *Nature Materials* **5**, 523 (2006), number: 7 Publisher: Nature Publishing Group.
- [27] S. Hellmann, K. Rossnagel, M. Marczynski-Bhlow, and L. Kipp, Vacuum space-charge effects in solid-state photoemission, *Physical Review B* **79**, 035402 (2009), publisher: American Physical Society.
- [28] M. Puppin, Y. Deng, O. Prochnow, J. Ahrens, T. Binhammer, U. Morgner, M. Krenz, M. Wolf, and R. Ernstorfer, 500 kHz OPCPA delivering tunable sub-20 fs pulses with 15 W average power based on an all-ytterbium laser, *Opt. Express* **23**, 1491 (2015).
- [29] See Supplemental Material at [URL will be inserted by publisher] for details on the sample preparation, the trARPES temporal resolution determination, the data normalization procedure, and the computational details for DFT. The Supplemental Material includes Refs. [12, 28, 83–85].
- [30] P. Giannozzi, S. Baroni, N. Bonini, M. Calandra, R. Car, C. Cavazzoni, D. Ceresoli, G. L. Chiarotti, M. Cococcioni, I. Dabo, A. D. Corso, S. de Gironcoli, S. Fabris, G. Fratesi, R. Gebauer, U. Gerstmann, C. Gougoussis, A. Kokalj, M. Lazzeri, L. Martin-Samos, N. Marzari, F. Mauri, R. Mazzarello, S. Paolini, A. Pasquarello, L. Paulatto, C. Sbraccia, S. Scandolo, G. Sclauzero, A. P. Seitsonen, A. Smogunov, P. Umari, and R. M. Wentzcovitch, QUANTUM ESPRESSO: a modular and open-source software project for quantum simulations of materials, *J. Phys.: Condens. Matter* **21**, 395502 (2009).
- [31] L. Hedin, New Method for Calculating the One-Particle Green's Function with Application to the Electron-Gas Problem, *Physical Review* **139**, A796 (1965), publisher: American Physical

Society.

- [32] F. Aryasetiawan and O. Gunnarsson, The GW method, *Rep. Prog. Phys.* **61**, 237 (1998).
- [33] J. M. Riley, F. Mazzola, M. Dendzik, M. Michiardi, T. Takayama, L. Bawden, C. Granerod, M. Leandersson, T. Balasubramanian, M. Hoesch, T. K. Kim, H. Takagi, W. Meevasana, P. Hofmann, M. S. Bahramy, J. W. Wells, and P. D. C. King, Direct observation of spin-polarized bulk bands in an inversion-symmetric semiconductor, *Nat. Phys.* **10**, 835 (2014), arXiv:1408.6778.
- [34] T. Finteis, M. Hengsberger, T. Straub, K. Fauth, R. Claessen, P. Auer, P. Steiner, S. Hüfner, P. Blaha, M. Vögt, M. Lux-Steiner, and E. Bucher, Occupied and unoccupied electronic band structure of WSe₂, *Phys. Rev. B* **55**, 10400 (1997).
- [35] J. M. Riley, W. Meevasana, L. Bawden, M. Asakawa, T. Takayama, T. Eknapakul, T. K. Kim, M. Hoesch, S.-K. Mo, H. Takagi, T. Sasagawa, M. S. Bahramy, and P. D. C. King, Negative electronic compressibility and tunable spin splitting in WSe₂, *Nat. Nanotechnol.* **10**, 1043 (2015).
- [36] I. Tanabe, T. Komesu, D. Le, T. B. Rawal, E. F. Schwier, M. T. Zheng, Y. Kojima, H. Iwasawa, K. Shimada, T. S. Rahman, and P. A. Dowben, The symmetry-resolved electronic structure of 2H-WSe₂(0001), *Journal of Physics-Condensed Matter* **28**, 10 (2016).
- [37] S. Hüfner, *Very high resolution photoelectron spectroscopy* (New York Springer, Berlin, 2007).
- [38] A. D. Katnani and G. Margaritondo, Microscopic study of semiconductor heterojunctions: Photoemission measurement of the valance-band discontinuity and of the potential barriers, *Physical Review B* **28**, 1944 (1983), publisher: American Physical Society.
- [39] S. Roth, A. Crepaldi, M. Puppini, G. Gatti, D. Bugini, I. Grimaldi, T. R. Barrilot, C. A. Arrell, F. Frassetto, L. Poletto, M. Chergui, A. Marini, and M. Grioni, Photocarrier-induced band-gap renormalization and ultrafast charge dynamics in black phosphorus, *2D Materials* **6**, 031001 (2019), publisher: IOP Publishing.
- [40] J. C. Fuggle, *Unoccupied Electronic States : Fundamentals for XANES, EELS, IPS and BIS* (Springer, Springer Berlin Heidelberg, Berlin Berlin, Heidelberg, 1992).
- [41] F. J. Himpsel, Inverse photoemission from semiconductors, *Surface Science Reports* **12**, 3 (1990).
- [42] N. D. Lang, Spectroscopy of single atoms in the scanning tunneling microscope, *Phys. Rev. B* **34**, 5947 (1986).

- [43] V. N. Strocov, Very low-energy electron diffraction as a method of band structure investigations: Applications in photoelectron spectroscopy, *Physics of the Solid State* **42**, 1973 (2000).
- [44] L. Hedin and S. Lundqvist, *Effects of Electron-Electron and Electron-Phonon Interactions on the One-Electron States of Solids* (Academic Press, 1970) pp. 1 – 181, iSSN: 0081-1947.
- [45] B. S. Kim, J.-W. Rhim, B. Kim, C. Kim, and S. R. Park, Determination of the band parameters of bulk 2H-MX₂ (M = Mo, W; X = S, Se) by angle-resolved photoemission spectroscopy, *Sci. Rep.* **6**, 36389 (2016).
- [46] C. Monney, M. Herzog, A. Pulkkinen, Y. Huang, J. Pelliciani, P. Olalde-Velasco, N. Katayama, M. Nohara, H. Takagi, T. Schmitt, and T. Mizokawa, Mapping the unoccupied state dispersions in Ta₂NiSe₅ with resonant inelastic x-ray scattering, *Physical Review B* **102**, 085148 (2020), publisher: American Physical Society.
- [47] C. Monney, K. J. Zhou, H. Cercellier, Z. Vydrova, M. G. Garnier, G. Monney, V. N. Strocov, H. Berger, H. Beck, T. Schmitt, and P. Aebi, Mapping of Electron-Hole Excitations in the Charge-Density-Wave System 1T–TiSe₂ Using Resonant Inelastic X-Ray Scattering, *Physical Review Letters* **109**, 047401 (2012), publisher: American Physical Society.
- [48] M. Traving, M. Boehme, L. Kipp, M. Skibowski, F. Starrost, E. E. Krasovskii, A. Perlov, and W. Schattke, Electronic structure of WSe₂: A combined photoemission and inverse photoemission study, *Phys. Rev. B* **55**, 10392 (1997).
- [49] A. R. Beal and W. Y. Liang, Excitons in 2H-WSe₂ and 3R-WS₂, *J. Phys. C: Solid State Phys.* **9**, 2459 (1976).
- [50] H. Zeng, G.-B. Liu, J. Dai, Y. Yan, B. Zhu, R. He, L. Xie, S. Xu, X. Chen, W. Yao, and X. Cui, Optical signature of symmetry variations and spin-valley coupling in atomically thin tungsten dichalcogenides, *Scientific Reports* **3**, 1608 (2013), number: 1 Publisher: Nature Publishing Group.
- [51] A. Arora, M. Koperski, K. Nogajewski, J. Marcus, C. Faugeras, and M. Potemski, Excitonic resonances in thin films of WSe₂ : from monolayer to bulk material, *Nanoscale* **7**, 10421 (2015), arXiv:arXiv:1503.01682v1.
- [52] R. Schuster, Y. Wan, M. Knupfer, and B. Büchner, Nongeneric dispersion of excitons in the bulk of WSe₂, *Phys. Rev. B* **94**, 1 (2016), arXiv:1604.01895.
- [53] A. Jain, S. P. Ong, G. Hautier, W. Chen, W. D. Richards, S. Dacek, S. Cholia, D. Gunter, D. Skinner, G. Ceder, and K. a. Persson, The Materials Project: A materials genome approach

- to accelerating materials innovation, *APL Materials* **1**, 011002 (2013).
- [54] R. Roldán, J. A. Silva-Guillén, M. P. López-Sancho, F. Guinea, E. Cappelluti, and P. Ordejón, Electronic properties of single-layer and multilayer transition metal dichalcogenides MX_2 ($\text{M} = \text{Mo}, \text{W}$ and $\text{X} = \text{S}, \text{Se}$) (2014), arXiv:1410.2154.
- [55] A. Kumar and P. K. Ahluwalia, Electronic structure of transition metal dichalcogenides monolayers 1H-MX_2 ($\text{M} = \text{Mo}, \text{W}$; $\text{X} = \text{S}, \text{Se}, \text{Te}$) from ab-initio theory: new direct band gap semiconductors, *The European Physical Journal B* **85**, 186 (2012).
- [56] W. Huang, X. Luo, C. K. Gan, S. Y. Quek, and G. Liang, Theoretical study of thermoelectric properties of few-layer MoS_2 and WSe_2 , *Physical Chemistry Chemical Physics* **16**, 10866 (2014), publisher: The Royal Society of Chemistry.
- [57] S. Curtarolo, W. Setyawan, S. Wang, J. Xue, K. Yang, R. H. Taylor, L. J. Nelson, G. L. W. Hart, S. Sanvito, M. Buongiorno-Nardelli, N. Mingo, and O. Levy, AFLOWLIB.ORG: A distributed materials properties repository from high-throughput ab initio calculations, *Computational Materials Science* **58**, 227 (2012).
- [58] H. Jiang, Electronic Band Structures of Molybdenum and Tungsten Dichalcogenides by the GW Approach, *The Journal of Physical Chemistry C* **116**, 7664 (2012).
- [59] J. He, K. Hummer, and C. Franchini, Stacking effects on the electronic and optical properties of bilayer transition metal dichalcogenides MoS_2 , MoSe_2 , WS_2 , WSe_2 , *Phys. Rev. B* **89**, 075409 (2014).
- [60] E. J. Baerends, O. V. Gritsenko, and R. v. Meer, The Kohn-Sham gap, the fundamental gap and the optical gap: the physical meaning of occupied and virtual Kohn-Sham orbital energies, *Physical Chemistry Chemical Physics* **15**, 16408 (2013), publisher: Royal Society of Chemistry.
- [61] F. Giustino, *Materials modelling using density functional theory : properties and predictions* (Oxford University Press, Oxford, 2014).
- [62] J. P. Perdew and M. Levy, Physical Content of the Exact Kohn-Sham Orbital Energies: Band Gaps and Derivative Discontinuities, *Physical Review Letters* **51**, 1884 (1983), publisher: American Physical Society.
- [63] T. Straub, K. Fauth, T. Finteis, M. Hengsberger, R. Claessen, P. Steiner, S. Hufner, and P. Blaha, Valence-band maximum in the layered semiconductor WSe_2 : Application of constant-energy contour mapping by photoemission, *Phys. Rev. B* **53**, 16152 (1996).

- [64] J. P. Perdew, Density functional theory and the band gap problem, *Int. J. Quantum Chem.* **28**, 497 (2009).
- [65] M. S. Hybertsen and S. G. Louie, Electron correlation in semiconductors and insulators: Band gaps and quasiparticle energies, *Phys. Rev. B* **34**, 5390 (1986).
- [66] M. Rohlfing and S. G. Louie, Electron-hole excitations and optical spectra from first principles, *Physical Review B* **62**, 4927 (2000), publisher: American Physical Society.
- [67] E. Perfetto, D. Sangalli, A. Marini, and G. Stefanucci, First-principles approach to excitons in time-resolved and angle-resolved photoemission spectra, *Physical Review B* **94**, 245303 (2016), arXiv: 1607.06449.
- [68] A. Rustagi and A. F. Kemper, Photoemission signature of excitons, *Physical Review B* **97**, 235310 (2018).
- [69] D. Christiansen, M. Selig, E. Malic, R. Ernstorfer, and A. Knorr, Theory of exciton dynamics in time-resolved ARPES: Intra- and intervalley scattering in two-dimensional semiconductors, *Physical Review B* **100**, 205401 (2019).
- [70] M. Weinelt, Time-resolved two-photon photoemission from metal surfaces, *J. Phys.: Condens. Matter* **14**, R1099 (2002).
- [71] J. Shah, *Ultrafast spectroscopy of semiconductors and semiconductor nanostructures* (Springer Verlag, Berlin New York, 2010).
- [72] S. Ulstrup, A. G. abo, J. A. Miwa, J. M. Riley, S. S. Grnborg, J. C. Johannsen, C. Cacho, O. Alexander, R. T. Chapman, E. Springate, M. Bianchi, M. Dendzik, J. V. Lauritsen, P. D. C. King, and P. Hofmann, Ultrafast Band Structure Control of a Two-Dimensional Heterostructure, *ACS Nano* **10**, 6315 (2016).
- [73] L. Waldecker, R. Bertoni, H. Hbener, T. Brumme, T. Vasileiadis, D. Zahn, A. Rubio, and R. Ernstorfer, Momentum-Resolved View of Electron-Phonon Coupling in Multilayer WSe₂, *Physical Review Letters* **119**, 036803 (2017), publisher: American Physical Society.
- [74] W. S. Yun, S. W. Han, S. C. Hong, I. G. Kim, and J. D. Lee, Thickness and strain effects on electronic structures of transition metal dichalcogenides: 2H-MX₂ semiconductors (M = Mo, W; X = S, Se, Te), *Physical Review B* **85**, 033305 (2012), publisher: American Physical Society.
- [75] M. Puppini, S. Polishchuk, N. Colonna, A. Crepaldi, D. N. Dirin, O. Nazarenko, R. De Gennaro, G. Gatti, S. Roth, T. Barillot, L. Poletto, R. P. Xian, L. Rettig, M. Wolf, R. Ernstorfer,

- M. V. Kovalenko, N. Marzari, M. Grioni, and M. Chergui, Evidence of large polarons in photoemission band mapping of the perovskite semiconductor CsPbBr_3 , *Phys. Rev. Lett.* **124**, 206402 (2020).
- [76] A. A. Mitioglu, P. Plochocka, . Granados del Aguila, P. C. M. Christianen, G. Deligeorgis, S. Anghel, L. Kulyuk, and D. K. Maude, Optical investigation of monolayer and bulk tungsten diselenide (WSe_2) in high magnetic fields, *Nano Letters* **15**, 4387 (2015).
- [77] J. R. Schaibley, H. Yu, G. Clark, P. Rivera, J. S. Ross, K. L. Seyler, W. Yao, and X. Xu, Valleytronics in 2D materials, *Nature Reviews Materials* **1**, 1 (2016), number: 11 Publisher: Nature Publishing Group.
- [78] F. A. Rasmussen and K. S. Thygesen, Computational 2D Materials Database: Electronic Structure of Transition-Metal Dichalcogenides and Oxides, *J. Phys. Chem. C* **119**, 13169 (2015).
- [79] R. P. Xian, V. Stimper, M. Zacharias, S. Dong, M. Dendzik, S. Beaulieu, B. Schlkopf, M. Wolf, L. Rettig, C. Carbocono, S. Bauer, and R. Ernstorfer, A machine learning route between band mapping and band structure (2020), arXiv:2005.10210 [physics.data-an].
- [80] J. Maklar, Y. W. Windsor, C. W. Nicholson, M. Puppini, P. Walmsley, V. Esposito, M. Porer, J. Rittmann, D. Leuenberger, M. Kubli, M. Savoini, E. Abreu, S. L. Johnson, P. Beaud, G. Ingold, U. Staub, I. R. Fisher, R. Ernstorfer, M. Wolf, and L. Rettig, Nonequilibrium charge-density-wave order beyond the thermal limit, *Nature Communications* **12**, 2499 (2021).
- [81] C. W. Nicholson, M. Puppini, A. Lcke, U. Gerstmann, M. Krenz, W. G. Schmidt, L. Rettig, R. Ernstorfer, and M. Wolf, Excited-state band mapping and momentum-resolved ultrafast population dynamics in In/Si(111) nanowires investigated with XUV-based time- and angle-resolved photoemission spectroscopy, *Physical Review B* **99**, 155107 (2019).
- [82] C. W. Nicholson, A. Lcke, W. G. Schmidt, M. Puppini, L. Rettig, R. Ernstorfer, and M. Wolf, Beyond the molecular movie: Dynamics of bands and bonds during a photoinduced phase transition, *Science* **362**, 821 (2018), publisher: American Association for the Advancement of Science Section: Report.
- [83] S. H. El-Mahalawy and B. L. Evans, The thermal expansion of $2H\text{-MoS}_2$, $2H\text{-MoSe}_2$ and $2H\text{-WSe}_2$ between 20 and 800°C , *Journal of Applied Crystallography* **9**, 403 (1976).
- [84] J. P. Perdew, K. Burke, and M. Ernzerhof, Generalized Gradient Approximation Made Simple, *Physical Review Letters* **77**, 3865 (1996), publisher: American Physical Society.

- [85] J. Deslippe, G. Samsonidze, D. A. Strubbe, M. Jain, M. L. Cohen, and S. G. Louie, Berkeleygw: A massively parallel computer package for the calculation of the quasiparticle and optical properties of materials and nanostructures, *Computer Physics Communications* **183**, 1269 (2012).